Reactive transport modeling of acetic acid-induced degradation in portland cement paste

Maximilian Löher [a],*, Neven Ukrainczyk [a], Andreas Bogner [b], Astrid Hirsch [b], Frank Dehn [b], Eduardus Koenders [a]

[a] Institute of Construction and Building Materials, Technical University of Darmstadt, Franziska-Braun-Straße 3, Darmstadt 64287, Hessen, Germany
[b] Institute of Concrete Structures and Buildings Materials, Department Building Materials and Concrete Construction, Karlsruhe Institute of Technology (KIT), Gotthard-Franz-Str. 3, Karlsruhe 76131, Baden-Württemberg, Germany

ARTICLE INFO

ABSTRACT

A reactive transport model was employed to investigate the influence of multiple hydrate phases during acetic acid attack on Portland cement paste. The simulation accounted for the dissolution of primary cement hydrates like Ettringite, Portlandite and C-S-H, along with the formation of silica gel products impacting diffusivity. The simulations primarily utilized independent material parameters, though the effective specific surface area of C-S-H phases required adjustment, indicating that only a small fraction is active in bulk paste compared to experimental values obtained from powders. Experiments involved exposing hardened cement paste samples to acetic acid (pH = 3) for durations ranging from 35 to 84 days. The model predicted changes in mineral assemblages, porosity, and pore solution chemistry versus degradation depth and time. Comparison of calculated Ca and Si-contents with experimentally obtained values from μXRF analysis demonstrated good agreement of within 6% error, highlighting the importance of considering multiple minerals.

1. Introduction

Cement-based materials have limited resistance to aggressive acidic environments, commonly encountered in containers for animal manure, silage in agriculture [1–3], the food industry [4], alternative energy structures using biogas or geothermal water [5,6], wastewater structures [7–9], cooling towers, downhole oil wells, and exposure to natural acid rains and carbonation. The performance of cementitious materials relies on their ability to withstand aggressive species ingress over time. Consequently, extensive alterations in phase assemblage composition and experimentally determined information about chemical reactions between aggressive species and various hydrated phases of cement paste are imperative. These thermodynamic and kinetic data inform reactive-transport models predicting prolonged cement-based materials deterioration under diverse acid exposures and boundary conditions.

In acid attacks, the pore solution pH decreases, disrupting the equilibrium in the cement paste matrix and rendering all cement phases thermodynamically unstable at pH values below 10 [4,9,10]. This leads to the dissolution or alteration (decalcification) of cement hydration products through hydrolytic decomposition, resulting in substantial material degradation. As degradation progresses, the affected layer thickens, thereby enhancing its protective capabilities and shifting

the dissolution reaction from a kinetically-controlled to a diffusion-controlled regime [2,10]. The effective diffusivity of acid species in the damaged material is typically an order of magnitude higher than in undamaged material [11,12]. Nitric and acetic acid attacks induce rapid degradation, forming a highly porous layer due to leaching of highly soluble calcium salts (nitrates and acetates) [1–4,10,11]. Conversely, slower degradation by acids forming low-solubility acid salts, like sulfuric acid, occurs through the precipitation of a protective layer (e.g., gypsum) blocking the pores [2,7–9]. The porous degraded layer has low mechanical strength and contains silica gel with a pore solution pH similar to the external acid. This layer also includes Brownmillerite (at pH 3 to 4), aluminum hydroxide gel (pH 3 to 4), and amorphous ferric hydroxide (pH 1 to 2), with the calcium salt of the acid determined by solubility and liquid saturation [1,13]. A transition zone, a mechanically sound region, experiences a gradual pH increase until reaching the undamaged core material value. With a drop in pore solution pH, Portlandite dissolves first, followed by calcium silicate hydrate (C–S–H), and calcium aluminate phases [1–4,10]. The depth of these zones depends on material composition, acid type, and solution concentration and saturation. Thermodynamic modeling [1,4,9,10] of acidification and leaching in cement and cement blended with silica

---

* Corresponding author.

E-mail addresses: loeher@wib.tu-darmstadt.de (M. Löher), ukrainczk@wib.tu-darmstadt.de (N. Ukrainczyk).
URL: http://www.wib.tu-darmstadt.de (M. Löher).

fume systems was comparatively studied in PHREEQC, utilizing the CSH3T solubility model [10,14], constructed from three C–S–H end members [10]. In a recent study, Roosz et al. [15] conducted a semi-batch experiment on OPC degradation by acetic acid, comparing results with thermodynamic predictions employing C–(A-)S–H phases, characterized by their Ca/Si and Al/Si ratios. While models accurately represented most liquid compositions, discrepancies in Si and Al at low pH revealed data gaps. NMR analysis identified an unexpected aluminosilicate gel, leading the study to propose a new composition and equilibrium constant for this phase.

Thermodynamic (TD) models, when integrated into reactive transport models, hold significant relevance for modeling experimental studies, such as those conducted by Dyer [16]. In his work, Dyer employed an inverse modeling approach to empirically estimate the apparent diffusion coefficient based on the pH increase observed in an external acidic solution. However, this approach did not account for the time-dependent or spatial variations in porosity, instead representing an averaged diffusion rate over the entire degradation period for both degraded and intact cement paste. This highlights the need for more accurate modeling that can capture the dynamic evolution of porosity and material properties over time. The integration of improved TD models into advanced reactive transport (RT) models is critical for enhancing predictive accuracy. RT models, which couple chemical thermodynamics and kinetics with diffusive and convective transport processes, possess the essential capability to predict and extrapolate complex degradation mechanisms in cement-based materials [17]. This makes them invaluable for forecasting the long-term performance and durability of such materials under aggressive environmental conditions.

However, their effectiveness hinges on a substantial set of input parameters and experimental data for accurate model calibration and validation. The parametrization of RT models, especially in the context of rarely studied degradation processes in cement-based systems, such as acetic acid attack, presents a particular challenge and demands validation tests. Limited predictive capabilities arise from the absence of crucial links between chemical reaction kinetics, pore structure changes, and ion mass transport in current modeling approaches [18, 19].

In prior investigations aimed at addressing this issue, various research teams initiated their modeling studies utilizing the software CrunchFlow [20], primarily concentrating on the carbonation process within cementitious structures. In these studies, the C–S–H-phases were simplified to a single phase coupled without considering phase conversions among the various C–S–H-phases [21–23].

This study aims to bridge the abovementioned research gaps and addresses identified limitations by developing a model that implements dissolution–precipitation kinetics of multiple C–S–H-phases and their phase conversions, offering a more comprehensive understanding of degradation mechanisms in cement-based systems. The fundamental parametrization approach proposed is validated by extensive experimental investigations.

2. Materials and methods

2.1. Materials and sample preparation

Hardened cement paste (hcp) with a water to cement mass ratio (w/c) of 0.35 was investigated. In each case, after mixing the solids and water with an IKA RE-166 stirrer (IKA-Werke GmbH & Co. KG, Staufen, Germany) at room temperature, a plastic bottle with a volume of one liter was completely filled with the resulting paste in three steps, always followed by densifying using a vibrating table. The sealed bottles were shaken for 24 h at room temperature in a Hei-MIX Reax 2 overhead shaker (Heidolph Instruments GmbH & Co. KG, Schwabach, Germany) to ensure a homogeneous hardening and afterwards stored at 20 °C. After at least 21 days, drilling cores with a diameter of either 10 mm or 50 mm and a thickness between 15

and 35 mm were prepared out of this hardened paste. The lateral surfaces of these drilling cores were embedded in epoxy resin (MC-DUR 1800, MC-Bauchemie Müller GmbH & Co. KG, Essen, Germany) and afterwards these samples were stored in a small volume of deionized water (water volume/sample surface <20 ml/cm^2) at 20 °C until the age of 28 days. The composition of the employed CEM I 42.5 R cement determined by X-ray fluorescence spectroscopy (XRF) and X-ray diffraction (XRD) is described in Berger et al. [10].

2.1.1. Acetic acid attack

The drilling cores (initially 13 small and four big drilling cores) with a diameter of 10 mm and 50 mm embedded in epoxy resin as described in 2.1 were at the age of 28 days placed in a box filled with 26 l of diluted acetic acid. The solution was continuously stirred and the pH value of the solution was kept constant at pH = 3 by continuous titration with an OMNIS titration system obtained by Deutsche METROHM GmbH & Co. KG (Filderstadt, Germany). Despite the experiment was carried out in an air-conditioned room at 20 °C, due to the heat development of the acid attack, the temperature of the solutions was approximately 25 °C. The solution was renewed after 3 days, and thereafter at 6 subsequent timepoints, to mitigate the accumulation of acetate ions and prevent the calcium ion concentration from exceeding 200 mg/L. Calcium ion concentrations were subsequently determined using microwave plasma atomic emission spectrometry (MP-AES), employing a 4100 MP-AES instrument from Agilent Technologies Deutschland GmbH (Waldbronn, Germany).

Sampling was conducted at 12 discrete time points and subsequently analyzed to elucidate the temporal evolution of the acid attack. The sampling of a small drilling core was conducted after: 7, 14, 21, 28, 35, 42, 49, 56, 63, 70, 77, and 84 days. In addition, at specific time points (28 days, 56 days, 70 days, and 84 days), a larger drilling core was extracted. Each time a sample was removed, the volume of the solution was adjusted to keep the ratio of volume of solution to the sample surface constant at approx. 180 cm^3/cm^2.

2.2. Methods

2.2.1. Micro X-ray fluorescence spectroscopy (µXRF)

After the acid attack, the drilling cores with a diameter of 10 mm were prepared for Micro X-ray fluorescence spectroscopy (µXRF) investigations by cutting along the direction of attack, afterwards embedding in epoxy resin (Epoxy 2000 resin and hardener from Cloeren Technology GmbH, Wegberg, Germany) under vacuum using a SimpliVac Vacuum System obtained by Buehler (ITW Test & Measurement GmbH, Leinfelden-Echterdingen, Germany) and finally polishing with an AutoMet 250 obtained by Buehler (ITW Test & Measurement GmbH, Leinfelden-Echterdingen, Germany). The polishing process is described in detail in Caron et al. [24].

The investigations were carried out with a Bruker M4 TORNADO µXRF instrument (Bruker Nano GmbH, Berlin, Germany) using a rhodium target to generate the high-energy radiation, a poly-capillary lens with a spot size of 25 µm and a 30 mm^2 silicon drift detector (SDD) for energy-dispersive detection of the fluorescence radiation. All measurements were performed under vacuum conditions at 20 mbar with an accelerating voltage of 50 kV and a current of 200 µA. The X-ray energy spectra were collected in the range 0–40 keV. The intensities of the following elements were obtained: Na, Mg, Al, Si, S, Cl, K, Ti, Mn and Fe. For each sample, 10 measurements were carried out along a line along the direction of attack with a resolution of 25 µm and a measurement time of 1 s per spot. The mean value of each of these 10 measurements was evaluated.

Since this method cannot detect elements lighter than Sodium, like Hydrogen, Carbon and Oxygen, the absolute contents of elements in the samples cannot be determined. Therefore, the change in content of the relevant elements relative to the unaltered inner part of the samples was investigated. For each sample, the measured intensity for a given element at each spot was normalized with the mean intensity for this element obtained for the unaltered part of this specific sample.

3. Reactive-transport mechanisms

3.1. Introduction

A reactive transport model (RTM) incorporating various mechanisms of mineral dissolution and precipitation is presented, wherein thermodynamic, kinetic, and transport processes are taken into account. As described by Brunet et al. [21] the challenges building such models are 3-fold:

- develop a reactive transport model under experimental constraints
- understand and quantify the role of hardened cement paste properties
- link the material composition with long-term behavior.

Within these systems the overall deterioration of the cement-based materials can be reaction rate or transport limited, depending on which is the rate determining step (RDS). This RDS can also vary within the temporal evolution of the simulation, depending on how the parameters change in the system. This dependence on reaction rate or transport limiting step can also be described by the Damköhler number $\left(Da_{II}\right)$ which gives the relation between surface reaction to diffusional transport [25].

A 1D numerical model based on transport, thermodynamics, and kinetics was developed in CrunchFlow [20] to address this issue. Omitting convective terms from the transport formulation simplifies the problem without compromising its fundamental characteristics. From reaction thermodynamics perspective, C–S–H solid solution modeling plays an important role in mineral modeling, allowing us to account for the formation and evolution of C–S–H-phases and their conversion to amorphous SiO_2.

3.2. Transport

3.2.1. Diffusion

The transport equation consists of diffusion, convection and reaction terms (sink/source), in which the convection term can be neglected if the model is diffusion controlled. The change of the microstructure is taken into account by adjusting the parameter by the local porosity, tortuosity and the effective diffusion coefficient [26].

$$\frac{\partial}{\partial t}\left(\Phi S_L C_i\right) = -\frac{\partial}{\partial x}\left(\Phi\, D_i^{\text{eff}} S_L \frac{\partial C_i}{\partial x}\right) + R_{ij} \tag{1}$$

with Φ as the porosity, C_i as the concentration of species i [mole/m^3], D_i^{eff} as effective diffusion coefficient of species i [m^2/s], S_L as the saturation index and R_{ij} as sink or source term from the reaction of species i with mineral j. The concentration should be corrected by ion activity coefficients, typically calculated using the extended Debye–Hückel equation, as a function of a molar ionic strength of the solution [27], valid for moderate concentrations of up to 1 or even 2 mol/L.

This formulation can be extended by the Nernst–Planck-Equation (NPE) to elucidate the transport behavior of charged species (ions) under the influence of both concentration gradients and applied electrical fields. This equation offers insight into the interplay between diffusion and migration processes for multiple ionic species within an electrolyte solution [28].

Mathematically, the NPE describes the relationship between the flux $\left(J_i\right)$ of a specific ionic species i, its concentration gradient $\left(\nabla C_i\right)$, the electrical potential (ψ), and the mobility $\left(D_i/(RT)\right)$ of that particular ion [26]:

$$J_i = -D_i\nabla C_i - \frac{z_i F D_i}{RT}C_i\nabla\psi \tag{2}$$

where J_i is the flux of species i, D_i is its diffusion coefficient, C_i is its concentration, z_i is its charge number, F is Faraday's constant, R is the gas constant, T is the temperature, and ψ is the electrical potential.

The NPE combines diffusion and migration (or electromigration) contributions to comprehensively depict intricate ionic systems involving numerous ion interactions. These mechanisms result in tightly linked variations in ionic strengths and diffusion concentrations.

3.2.2. Porosity

The porosity of the bulk medium is determined by summation of the volume fractions of each mineral (Φ) [26,29]:

$$\Phi^{\text{bulk}} = 1 - \sum_{j=1}^{N}\Phi_j \tag{3}$$

where N represents the number of minerals in the mixture and Φ_j represents the volume fraction of each mineral in m^3 mineral per m^3 medium. This expression accounts for the fact that the total porosity is equal to unity minus the combined volumes occupied by each individual mineral. Consideration of the volume fractions and the resulting porosity in each cell and at each time step enables incorporation of temporal and spatial variations in the diffusional transport mechanism. Porosity changes and volume fraction dynamics are tightly coupled; consequently, updates to the porosity values occur simultaneously with modifications to the composition of the material. This approach provides a comprehensive representation of the interplay between porosity, mineralogy, and transport properties, enabling improved prediction of transport behavior throughout the cementitious material.

Within the conversion of one mineral to the other, not only the gain and loss of the mineral need to be considered but also the change of molar volumes [22]:

$$\Phi_{jk}^{(t+\delta t)} = \Phi_{jk}^{(t)} + \underbrace{V_j}_{\substack{\text{molar volume}\\\text{of mineral } j}} \cdot \underbrace{r_{jk}^{(t+\delta t)}}_{\substack{\text{volumetric}\\\text{reaction rate}}} \cdot \delta t \tag{4}$$

Here, the evolution of mineral formation can be quantified via changes in porosity (Φ). For the following time step $(t+\delta t)$, the updated porosity $\left(\Phi_{jk}^{(t+\delta t)}\right)$ for a specific mineral phase (j) and computational element (k) is determined by accounting for the generated molar volumes of the minerals $\left(V_j^{mole}\right)$ and their respective reaction rates $\left(r_{jk}^{(t+\delta t)}\right)$.

3.2.3. Tortuosity

To address the evolving effective diffusion coefficient due to changes in microstructure and porosity an exponential form based on Archie's Law can be used [21,22,26]:

$$D_i^{\text{eff}} = \Phi^{\kappa}\, D_i^{\text{water}} \tag{5}$$

where Φ denotes the porosity, κ is the cementation factor, D_i^{eff} represents the effective diffusion coefficient of specie i, and D^{water} refers to the initial diffusion coefficient in water of specie i.

A cementation exponent of $\kappa = 4.8$ [–] is adopted, consistent with the value previously used by Brunet et al. [21]. With this parametrization, the effective diffusion coefficient varies significantly with porosity, accounting for the impact of tortuosity on transport rates.

3.3. Reaction

3.3.1. Reaction equation

Several researchers [21–23,30,31] have previously investigated the behavior of cement-based materials under chemical attack, including phases in the simulation like calcium hydroxide (CH), calcium silicate hydrate (C–S–H) and calcite $\left(CaCO_3\right)$. Mostly they were dealing with the interaction of wellbore cement and CO_2.

Despite these efforts, many limitations remain, particularly concerning the characterization of C–S–H-phases. In prior studies, C–S–H has been treated as a single entity, despite the existence of numerous distinct C–S–H-phases with varied Ca/Si-ratios, specific surface areas (SSA), and reaction kinetics. These differences can impact the rate and
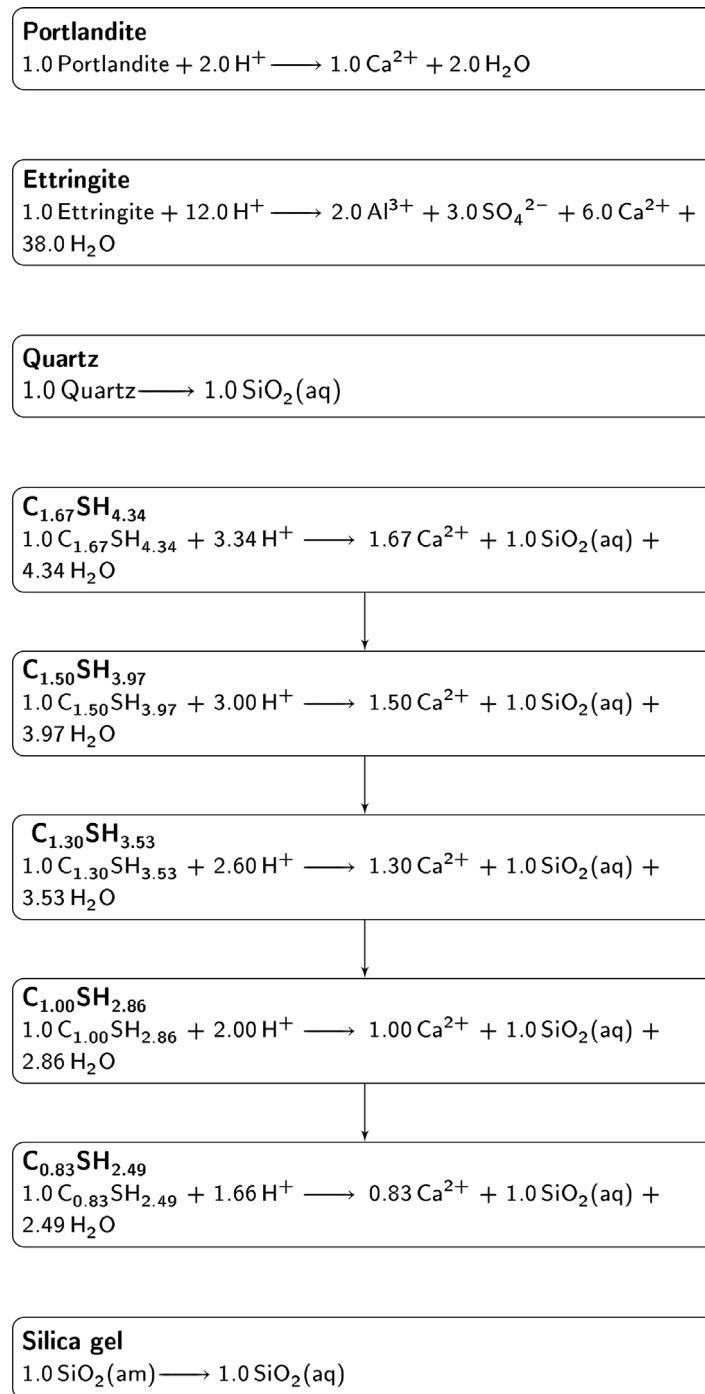
Portlandite
$$1.0 \, \text{Portlandite} + 2.0 \, \text{H}^+ \longrightarrow 1.0 \, \text{Ca}^{2+} + 2.0 \, \text{H}_2\text{O}$$

Ettringite
$$1.0 \, \text{Ettringite} + 12.0 \, \text{H}^+ \longrightarrow 2.0 \, \text{Al}^{3+} + 3.0 \, \text{SO}_4{}^{2-} + 6.0 \, \text{Ca}^{2+} + 38.0 \, \text{H}_2\text{O}$$

Quartz
$$1.0 \, \text{Quartz} \longrightarrow 1.0 \, \text{SiO}_2(\text{aq})$$

$C_{1.67}SH_{4.34}$
$$1.0 \, \text{C}_{1.67}\text{SH}_{4.34} + 3.34 \, \text{H}^+ \longrightarrow 1.67 \, \text{Ca}^{2+} + 1.0 \, \text{SiO}_2(\text{aq}) + 4.34 \, \text{H}_2\text{O}$$

$C_{1.50}SH_{3.97}$
$$1.0 \, \text{C}_{1.50}\text{SH}_{3.97} + 3.00 \, \text{H}^+ \longrightarrow 1.50 \, \text{Ca}^{2+} + 1.0 \, \text{SiO}_2(\text{aq}) + 3.97 \, \text{H}_2\text{O}$$

$C_{1.30}SH_{3.53}$
$$1.0 \, \text{C}_{1.30}\text{SH}_{3.53} + 2.60 \, \text{H}^+ \longrightarrow 1.30 \, \text{Ca}^{2+} + 1.0 \, \text{SiO}_2(\text{aq}) + 3.53 \, \text{H}_2\text{O}$$

$C_{1.00}SH_{2.86}$
$$1.0 \, \text{C}_{1.00}\text{SH}_{2.86} + 2.00 \, \text{H}^+ \longrightarrow 1.00 \, \text{Ca}^{2+} + 1.0 \, \text{SiO}_2(\text{aq}) + 2.86 \, \text{H}_2\text{O}$$

$C_{0.83}SH_{2.49}$
$$1.0 \, \text{C}_{0.83}\text{SH}_{2.49} + 1.66 \, \text{H}^+ \longrightarrow 0.83 \, \text{Ca}^{2+} + 1.0 \, \text{SiO}_2(\text{aq}) + 2.49 \, \text{H}_2\text{O}$$

Silica gel
$$1.0 \, \text{SiO}_2(\text{am}) \longrightarrow 1.0 \, \text{SiO}_2(\text{aq})$$

Fig. 1. Mineral phases used in the simulation.

extent of decalcification, and considering them will lead to a more realistic understanding.

To overcome this limitation, a previously well-defined batch reaction of a cement paste under acetic acid attack was simulated [10] containing, additionally to CH, amorphous SiO_2, Quartz, Ettringite, and five distinct C–S–H-phases as described in [32]: $C_{1.67}SH_{4.34}$, $C_{1.50}SH_{3.97}$, $C_{1.30}SH_{3.53}$, $C_{1.00}SH_{2.86}$ and $C_{0.83}SH_{2.49}$. Here the number refers to the molar content at constant Si-content. Each phase exhibits unique characteristics, including distinct Ca/Si-ratio, SSA, and dissolution behavior. The used mineral phases including the C–S–H-phases are shown in Fig. 1. Incorporating these five C–S–H-phases into the model is expected

to provide a more comprehensive understanding of the decalcification process, potentially yielding new insights into the underlying chemistry and physics. This approach may also enhance the understanding of the complex relationships between C–S–H-phases, pore structure, and deterioration processes.

3.3.2. Dissolution–precipitation behavior

Solid solution transformation refers to the gradual replacement of one mineral component with another [33]. Understanding the mechanisms behind this process is crucial for developing systems including

several minerals like cementitious materials. When modeling the deterioration of C–S–H-phases, it is crucial to simulate the sequential transformation of one phase to the next, accounting for the resulting changes in Ca/Si-ratio. This sequential approach enables the accurate representation of calcium dissolution from the mineral phases, which is a critical aspect of the deterioration process.

In this simulation the transition of the phases is implemented as complete dissolution and precipitation process. This interrelated processes with individual dissolution constants and dissolution kinetics govern the mineral transition. These constants are influenced by local environment eg. temperature, pH-value and local species. Due to the lack of values for some parameters (namely, the precipitation rate constant and effective surface areas), a fitting to stability and accuracy was necessary. The precipitation rates of the C–S–H-phases were kept same in this simulation. The parameters used are listed in Table 1.

By using the distinct solubility constants and dissolution kinetics it is possible to simulate a more realistic system to understand the temporal evolution of the distinct phases.

3.3.3. Transition State Theory (TST)

Mineral reactivity kinetics can be described by the Transition State Theory (TST). This theory provides a general reaction rate equation that can be employed to model reaction kinetics [20]:

$$R = Ak \left(a_{H^+} \right)^\alpha \left(1 - \frac{IAP}{K_{eq}} \right) \qquad (6)$$

where R is the reaction rate $\left[\text{mole/s} \right]$, A is the reactive surface area $\left[\text{m}^2 \right]$, k is the rate constant $\left[\text{mole/m}^2\text{s} \right]$, a_{H^+} is the activity of H^+, α is the rate dependency, K_{eq} is the solubility product, and IAP is the ion activity product. By incorporating the rate dependency on H^+, the non-linear dissolution behavior by acids can be captured. The term $\left(1 - IAP/K_{eq} \right)$ determines the reaction direction in terms of dissolution or precipitation. When this term is negative, the solution is supersaturated, indicating that the mineral will precipitate. On the other hand, a positive term indicates undersaturated solutions, suggesting that mineral dissolution will take place. The temperature dependence of the rate constant is determined utilizing the Arrhenius equation, setting 25 °C as the reference temperature [20].

3.3.4. Specific Surface Area (SSA)

The definition of specific surface areas (SSA) for individual minerals are associated with uncertainties caused by the lack of reliable information, especially when it comes to different C–S–H-phases with different Ca/Si-ratios. The values used for the SSA of C–S–H-phases vary and because researchers only used one single C–S–H-phase, the change in SSA could not be resolved. Suda et al. [34] synthesized hydration products with different Ca/Si-ratios and build a regression function to predict the SSA dependent of the Ca/Si-ratio.

According to this, the Specific Surface Area (SSA) in $\left[\text{m}^2/\text{g} \right]$ can be calculated [34]:

$$SSA_{C-S-H} = 269.3 - 325.1 \, log \left(\frac{Ca}{Si} \right) \qquad (7)$$

4. Simulation framework

Geochemical modeling plays a critical role in understanding the behavior of minerals. The usage of geochemical frameworks can easily be applied to cement-based materials chemistry. Besides CrunchFlow, there are several geochemical frameworks available, e.g. PHEEQC, MIN3P and PFLOTRAN.

PHREEQC was already used by several researchers to model the cement chemistry. Due to the usage of other researchers there already exists a database for cementitious systems [27]. The limitations here lying in the 1D-only simulation and the missing porosity–permeability coupling to update the temporal and local change of transport behavior [26]. CrunchFlow [20] has these features so that the transient

simulation of cement with updated porosity could excel in tackling transient scenarios. Constraints of CrunchFlow are the single-liquid phase and the missing parallelization, limiting their applicability to large systems or distributed computing environments. Therefore, more complex simulation need special work to couple CrunchFlow with parallelized transport frameworks (eg. Computational Fluid Dynamic (CFD) frameworks) to couple highly parallel transport solvers with the chemical reactions and porosity update capabilities of CrunchFlow. One approach in this field was already done by Beisman et al. [35].

An extensive review of the available geochemical frameworks is available in Steefel et al. [26].

4.1. CrunchFlow

In this investigation, CrunchFlow [20] – developed at the Lawrence Berkeley National Laboratory – was applied to address simultaneous reaction and transport challenges in porous media. Capable of solving energy, momentum, and mass conservation equations, CrunchFlow precisely captures complex chemico-physical phenomena in porous and fluid domains [20,26]. Widely utilized in geochemical studies, it has been adopted for dissolution processes in cement-based materials, such as wellbore cement and reactions with CO_2 [21,23,26].

CrunchFlow employs Finite Volume Method (FVM) to integrate Partial Differential Equations (PDEs) from transport and reaction kinetics. Transport computed via: (1) Fick's law with uniform diffusion coefficients or (2) Nernst–Planck-Equation with individual diffusion coefficients, accommodating accelerated/retarded transport [26].

The database can effortlessly incorporate customized reactions, including unique C–S–H-phases and their thermodynamics/kinetics. Its capacity accommodates even complex environments with an unlimited number of reactions.

4.1.1. Local densities/porosities

While the local porosity is defined as the local fraction of bulk in a volume, the local density is defined by the sum of all volume fractions including their specific density, which changes between different minerals.

The local porosity (Φ) refers to the ratio of pore space within a given volume to that same volume. This quantification represents the portion of the total volume occupied by voids or interstitial spaces.

Conversely, the local density (ρ^{ges}) signifies the mass per unit volume encompassed within that particular volume. It is determined by calculating the summation of individual volume fractions $\left(V_j \right)$ for each mineral phase present, multiplied by their respective specific densities. Thus, the relationship can be expressed as follows:

$$\rho^{ges} = \sum_{j=1}^{N} \left(V_j \cdot \rho_j \right) \qquad (8)$$

CrunchFlow updates porosity at each timestep, adapting local transport properties. It calculates mineral volume fragments with differing molar volumes, allowing precise monitoring of porosity shifts, e.g. denser calcite layers decreasing local transport speeds.

The influence of local densities exerts a significant impact on both transportation processes and chemical reactions. For instance, an increased density layer may hinder the penetration of acids, thereby decelerating the global reaction rate.

This update is done by calculating first the local porosity incorporating all bulk minerals (Eqs. (4) and (3)) and then derives the effective diffusion coefficient $\left(D^{\text{eff}}, \text{Eq. (5)} \right)$.

The reactive surface area (A) in each grid block k for the reaction in Eq. (6) is updated in Crunchflow involving also the local porosity and local volume fractions of the mineral j at time t according to the following equation [20–22]:

- Primary minerals, initially characterized by the user through volume fraction and specific surface area (SSA)
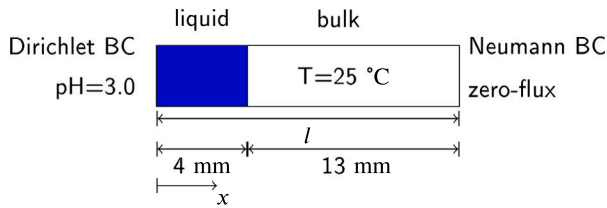
Fig. 2. Illustration of the 1D simulation domain.

$$A_{k,j}^t = A_{k,j}^0 \begin{cases} \dfrac{\Phi_k^t}{\Phi_k^0}\left(\dfrac{\Phi_{kj}^t}{\Phi_{kj}^0}\right)^{2/3}, & \text{dissolution} \\[3mm] \left(\dfrac{\Phi_{kj}^t}{\Phi_{kj}^0}\right)^{2/3}, & \text{precipitation} \end{cases} \qquad (9)$$

- Secondary minerals, initially characterized by a volume fraction of zero

$$A_{k,j}^t = A_{k,j}^0 \begin{cases} \left(\dfrac{\Phi_k^t}{\Phi_k^0}\Phi_{kj}^t\right)^{2/3}, & \text{dissolution} \\[3mm] \left(\dfrac{\Phi_{kj}^t}{\Phi_{kj}^0}\right)^{2/3}, & \text{precipitation} \end{cases} \qquad (10)$$

4.1.2. Primary species/Secondary species

CrunchFlow is using the canonical form for the reactions. In this form the species are split into primary and secondary species. Secondary species refer to the concentrations of the products or the amount of reactions in the system while primary species refer to the chemical elements. Secondary species can therefore be written as a combination of primary species. With this method the number of equations can be reduced to the number of secondary species [26,29,36–38].

4.1.3. Kinetic reaction options

As described before in the TST formulation of Eq. (6) the kinetics of dissolution and precipitation is dynamically controlled by over- and undersaturation. Considering different kinetics for dissolution and precipitation this equation needs to be formulated for both reactions separately. For this situation it is possible to define separate kinetics for the reversible reaction in which the same formulation as in Eq. (6) is used separately for dissolution and precipitation but always one mechanism being suppressed [20].

5. Case setup

5.1. CrunchFlow

In the given study, a computational simulation was executed for the Portland cement (PC) mixture previously described by Berger et al. [10]. The liquid phase within this system was maintained at a consistent pH value of 3.0, which included the presence of acetic acid. To allow a better representation of concentration gradients' development on the surface, both the solid and liquid regions were modeled in the simulation. This approach enabled the interface between them to dynamically adjust through dissolution and precipitation processes.

Further specifying the system, appropriate initial and boundary conditions are necessary, shown in Fig. 2.

The domain is split into a liquid domain of $l_{\text{liquid}} = 4\,\text{mm}$ and a solid domain which represents the cement specimen of $l_{\text{solid}} = 13\,\text{mm}$. During the experiments a maximum length of around $10\,\text{mm}$ was influenced by the acid attack so that a length of $13\,\text{mm}$ was chosen to be able

to show all changes. In this study, the spatial domain is discretized into individual elements of size $\delta l = 0.1\,\text{mm}$. Consequently, the entire domain encompasses a total number of 170 elements. The automated time discretization functionality of CrunchFlow managed the temporal resolution of the simulation, ensuring convergence up until the maximal duration of 84 days.

5.1.1. Region compositions and physical parameters

Our model incorporates nine minerals, including calcium hydroxide (Portlandite) CH, five C–S–H-phases, Quartz, Ettringite and amorphous SiO_2. Each mineral is described through thermodynamic and kinetic parameters. Accounting for phase equilibria among multiple solid phases enables the simulation of coexisting mineral assemblies.

The C–S–H-phases are used from Trapote-Barreira et al. [32] in which the volumetric fractions are calculated from the densities $\left(\text{C–S–H} = 2.7580 \text{ and } \text{CH} = 2.2414\,\text{g/cm}^3\right)$. Increments of Ca/Si-ratios used (1.67, 1.5, 1.3, 1.0, 0.83), were in a stepping of around 0.2 from the highest value of 1.67 to the lowest of 0.83.

In approaching nearer to the authentic system, quantities of Ettringite and Quartz were incorporated. The inclusion of Ettringite serves as a bridge between a complete representative composition, which would include all aluminate phases, while maintaining a manageable number of variables within a simplified model.

Over the whole simulation the temperature was set to constant 25 °C and the saturation to 1.0. The cementation factor κ is used from [21,22] and set to 4.8 [–].

In Table 1 the dissolution and precipitation rate is given in logarithmic scale and also the used H^+-dependency (α) for Eq. (6) is shown. In the last column the initial mineral composition leaned on Berger et al. [10] is shown. To simplify the model, the additional phases from Berger et al. [10] to the ones existing in the current model are summarized in the first C–S–H-phase $\left(C_{1.67}SH_{4.34}\right)$.

Table 2 presents the diffusion coefficients (D) and initial concentrations (C) of various species in solution. The presented concentrations, in conjunction with the diffusion coefficients, provide valuable insights into the spatial distribution of species within the solution. Concentration signifies the quantity of a substance existing per mass [mole/kg]. This concentration is then in CrunchFlow internally converted to [mole/m^3] to fit Eq. (1). In Table 2, also the concentrations are reported for both the pore solution and the acetic solution, which has been adjusted to achieve a required pH value of 3.0. The corresponding hydrogen ion concentration $\left(H^+\right)$ required to attain the specified pH level has been computed by CrunchFlow.

Referencing Leaist and Lyons [39], an identical diffusion coefficient value has been assigned for the diffusion of acetic acid, acetate, and their associated complexes.

The thermodynamic parameters such as molar volumes $\left(V^{mole}\right)$, molar masses (M), solubility product $\left(K_{sp}\right)$, and stoichiometric coefficients are presented in Table 3. Molar volumes signify the space occupied by one mole of a substance, while molar masses indicate the total mass of one mole of a mineral in [g/mole]. Solubility products quantify the equilibrium constant for the dissociation of the minerals, providing the saturation state for Eq. (6). Stoichiometric coefficients specify the ratio of reactants and products involved in balanced chemical equations, also providing quantities of species for post-processing.

5.2. Post-processing

In order to facilitate compatibility between the outcomes generated from μXRF experiments and simulation results, it is essential to implement post-processing procedures.

The primary function of μXRF lies in surface elemental analysis, providing an elemental mapping along a specified line. To ensure consistency between experimental data and simulated results, both sets must be subjected to equivalent data treatment processes. This

Table 1
Kinetic parameters/Mineral composition.

Mineral	Dissolution rate	Precipitation rate	Kinetic	SSA		H$^+$-dependency	Composition
	$log\ k$ [mole/m^{2}s]	$log\ k$ [mole/m^{2}s]	Mechanism	Calibrated [m^2/g]	Theoretical	α	V_j [Vol %]
Portlandite	−7.0[e]		TST	2.0	16.5[b]	–	0.066
C$_{1.67}$SH$_{4.34}$	−8.364[d]	−7.00[a]	D/P	4.0	196.9[c]	0.03[a]	0.566
C$_{1.50}$SH$_{3.97}$	−8.535[d]	−7.00[a]	D/P	4.0	212.1[c]	0.03[a]	0.01
C$_{1.30}$SH$_{3.53}$	−9.569[d]	−7.00[a]	D/P	1.0	232.3[c]	0.03[a]	0.01
C$_{1.00}$SH$_{2.86}$	−10.940[d]	−7.00[a]	D/P	4.0	269.3[c]	0.03[a]	0.01
C$_{0.83}$SH$_{2.49}$	−10.983[d]	−7.00[a]	D/P	4.0	295.6[c]	0.03[a]	0.01
SiO$_2$(am)	–	−12.00[a]	P	4.0		–	0.00
Quartz	−13.39[f]		TST	4.0		–	0.01
Ettringite	−10.00[a]		TST	1.0		–	0.10

(D/P): Separate formulation of dissolution and precipitation; (P): Precipitation only; (TST): dissolution/precipitation in both directions;

[a] Fitted value;

[b] [22];

[c] [34];

[d] [32]

[e] Proximate to [22,23];

[f] CrunchFlow database.

Table 2
Primary and Secondary species.

Specie	Diffusion coefficient D_i [m^2/s]		Concentrations C_i [mole/kg]	
	Value	Ref.	Acetic solution	Pore solution
Primary species				
H$^+$	9.310E−09	[23]	1.082E − 03	2.498E − 12
Ca^{2+}	0.793E−09	[40]	9.182E − 11	2.2943E − 02
Cl$^-$	2.03E−09	[40]	1.000E − 10	1.0000E − 10
K$^+$	1.96E−09	[40]	1.000E − 10	1.0000E − 03
Na$^+$	1.33E−09	[40]	1.000E − 10	1.0000E − 02
Al$_3{}^+$	0.559E−09	[23]	1.000E − 10	3.0512E − 23
AlO$_2{}^-$	1.0E−09[a]	–	1.000E − 10	1.0000E − 06
Fe$_3{}^+$	0.604E−09	[23]	1.000E − 10	1.0000E − 06
SO$_4{}^{2-}$	1.23E−09	[23]	1.000E − 10	9.9985E − 07
Acetic Acid (aq)	1.3E−09	[39]	6.867E − 01	1.0000E − 10
SiO$_2$ (aq)	0.921E−09	[22]	1.001E − 10	1.8475E − 07
Secondary species				
OH$^-$	5.270E−09	[40]	1.117E − 11	5.886E − 03
Acetate	1.3E−09	[39]	1.331E − 02	9.147E − 11
Ca(CH$_3$COO)$_2$(aq)	1.3E−09	[39]	1.297E − 12	8.184E − 21
CaCH$_3$COO$^+$	1.3E−09	[39]	7.359E − 12	8.529E − 12

[a] fitted value

involves consideration of the material's changing local density and normalization to the reference state within the undamaged region.

Initially, the individual elemental quantities associated with every mineral phase present in the simulation output require extraction. Subsequently, the conversion from volume to mass values should be adjusted based on their corresponding local densities and normalized relative to the undamaged bulk.

The calculation of the normalized mineral fractions entails the multiplication of the mineral volume $\left(V_j\right)$ obtained from the simulation, the mineral density $\left(\rho_j\right)$, the stoichiometric fraction $\left(n_{ji}\right)$ of the particular element within each mineral, and the element density $\left(\rho_i\right)$. The mineral density can be determined using its molar volume $\left(V_j^{mole}\right)$ and molar mass $\left(M_j\right)$. The elemental content $\left(\Omega_{ji}\right)$ in each mineral phase can then be written as:

$$\Omega_{ji} = V_j * \frac{\rho_j}{V_j^{mole}} \cdot \frac{n_{ji} \cdot \rho_i}{\rho_j} \tag{11}$$

Once these calculations have been performed for all minerals within each computational cell, the resulting fractions are aggregated and subsequently normalized to the final node to align them with the undamaged domain conditions.
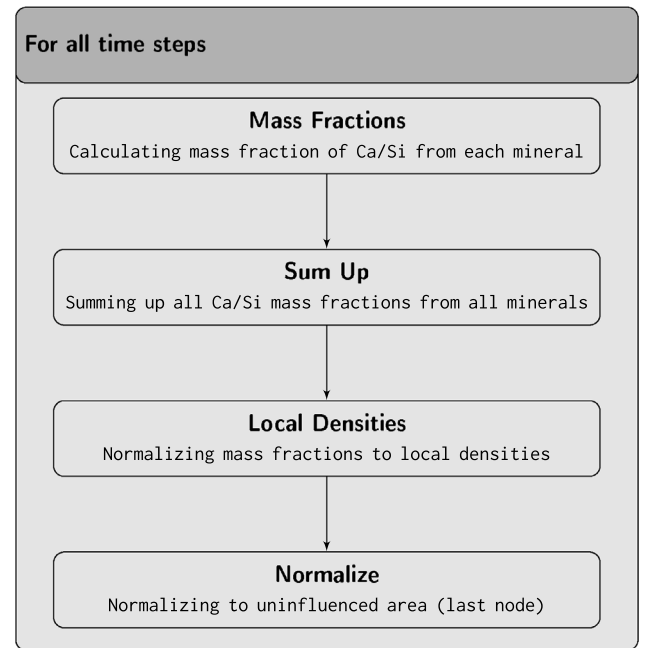

Fig. 3. Post-processing to obtain local Ca/Si amounts from.

These steps are shown in Eqs. (12), (13) and illustrated in Fig. 3.

$$\Omega_i = \left(\frac{\sum_{j=1}^{N} \Omega_{ji}}{\rho_k} \right) \tag{12}$$

$$\Omega_i^{norm}(x) = \frac{\Omega_i(x)}{\Omega_i(\text{last node})} \tag{13}$$

In the given system, calcium (Ca) and silicon (Si) serve as the primary constituents for evaluating its performance. These elements were selected due to their distinct stoichiometric content in the minerals. Through the integration of varying volume and mass fraction data, coupled with density modifications, a comprehensive evaluation of multiple mineral phases system's interactions can be accomplished.

5.2.1. Quantifying the results with masked RMSE

In order to assess the discrepancy between simulated and experimentally obtained data, the Root Mean Square Error (RMSE) was employed as a quantitative metric for comparison. Specifically, the Ca and Si content derived from experimental analyses and that calculated

Table 3
Thermodynamic values.

Mineral	Molar volume	Molar mass	Solubility product	Stoichiometric coefficients					
	V_i^{mole} [cm^3/mole]	M_i [g/mole]	K_{sp} at 25 °C	Ca^{2+}	SiO$_2$	H$^+$	H$_2$O	Al^{3+}	SO$_4{}^{2-}$
Portlandite	33.056[b]	74.0927[b]	20.1960[b]	1.00	0.0	−2.00	2.00	0.0	0.0
C$_{1.67}$SH$_{4.34}$	73.181[a]	201.834	29.133[c]	1.67	1.0	−3.34	4.34	0.0	0.0
C$_{1.50}$SH$_{3.97}$	68.418[a]	188.698	25.328[c]	1.50	1.0	−3.00	3.97	0.0	0.0
C$_{1.30}$SH$_{3.53}$	62.784[a]	173.159	20.950[c]	1.30	1.0	−2.60	3.53	0.0	0.0
C$_{1.00}$SH$_{2.86}$	54.268[a]	149.670	14.583[c]	1.00	1.0	−2.00	2.86	0.0	0.0
C$_{0.83}$SH$_{2.49}$	49.505[a]	136.534	11.150[c]	0.83	1.0	−1.66	2.49	0.0	0.0
SiO$_2$(am)	29.000[b]	60.0843[b]	−2.7136[b]	0.00	1.0	−4.00	2.00	0.0	0.0
Quartz	22.6880[b]	60.0843[b]	−4.0000[b]	0.00	1.0	−4.00	2.00	0.0	0.0
Ettringite	715.00	1279.2947	62.5362[b]	6.00	0.0	−4.00	2.00	2.00	3.0

[a] calculated with density from [32];

[b] CrunchFlow database;

[c] [32].

following post-processing of the simulation outcomes were contrasted. Subsequently, these sets of Ca and Si contents were treated as vectors to compute the RMSE value for each individual cell. With this method the accuracy can be evaluated quantitatively.

The RMSE can be calculated by:

$$RMSE = \sqrt{\frac{\sum_{k=1}^{N}\left(y_k - \hat{y}_k\right)^2}{N-1}} \qquad (14)$$

with y_k as the simulation result of point k, $\hat{y}_k$ as the experimental result of point k, and N as the total number of data points.

While the RMSE is unit dependent, the normalized values are used so that the output can be directly used as percentage of accuracy.

The Root Mean Squared Error (RMSE) was narrowed to the masked Root Mean Squared Error (mRMSE) as a metric for evaluating the discrepancy between predicted and measured values within specified domains. This approach was adopted due to the presence of non-representative or non-existing experimental data points, specifically those originating from experimental regions exhibiting features such as material loss. The omission of these data points from the RMSE calculation enabled the derivation of an error value that accurately represented the model's performance in the regions of interest that were most pertinent and significant. Consequently, the mRMSE assessment was carried out exclusively on the specified, unimpaired areas. Further details about the used domains are shown in Fig. 8 and Table 4.

Fig. 4 presents the comprehensive schematic representation of the modeling workflow using CrunchFlow and post-processing.

6. Results

The objective of this chapter is to elucidate the outcomes of the CrunchFlow model implementation, followed by a comparative analysis with experimental results. As previously described, the degradation of cement is not determined by a singular parameter; hence, the consideration of diverse spatial and temporal parameter fields becomes important. A description of various parameters and comparisons at distinct time intervals will be presented.

One essential parameter to investigate is the porosity, which plays a critical role in transportation processes, notably influencing variabilities in diffusional transport, as evidenced by Eq. (1). The temporal development of the porosity signifies the transition from a denser cement matrix to a less dense architecture. Consequently, this information provides initial insights into how porosity modifications affect transport mechanisms.

In the depicted representation, denoted as Fig. 5(a), the porosity values show an authentic progression despite the limitation in achieving such fine-grained measurements for this parameter.

The pH-value exhibits analogous characteristics to porosity, a property that cannot be precisely quantified in the bulk yet remains an essential parameter for evaluating the validity of mechanistic outcomes.

In Fig. 5(b), it can be seen that the dissolution of Portlandite was not in thermodynamical equilibrium, leading to further dissolution with the result of an elevation of the bulk pH-value relative to its initial condition. Sequential leaching of dissolved Portlandite to the liquid domain results in a decrease of the pH-value from the acetic liquid into the bulk phase. Concurrently, an increase of the pH-value in the liquid phase occurs near the solid–liquid interface.

The increase of the pH value in the liquid phase induces a modification of the pH gradient, which, in turn, influences the transport of species, thereby impacting the overall process dynamics. Consequently, simulating both the solid and liquid domains enables the emergence of a more realistic, self-organized distribution of concentration fields for all species. These findings underscore the significance of modeling both the bulk and liquid phases to accurately capture the complexities of the system and replicate its behavior with fidelity.

6.1. Mineral composition

The mineral composition holds particular significance in this simulation, given that one of the primary objectives is to model the interaction of various C–S–H-phases. Consequently, highlighting the sequential conversion of mineral phases becomes crucial. Fig. 6 illustrates all individual mineral phases at discrete time steps.

Fig. 7 presents a detailed illustration of the mineral phases within the affected zone at 84 days of acetic attack. Notably, Portlandite $(Ca(OH)_2)$ exhibits the most rapid consumption during this process, leading to substantial modifications in the system's chemical makeup. With the depletion of rapidly reacting Portlandite, the primary drivers for dissolution shift towards the transformation of C–S–H-phases and the precipitation of amorphous SiO_2.

Despite the lack of discernible variations in total porosity after the first big porosity increase, as depicted in Fig. 5(a), it should be noted that mineral conversions persist in its absence.

6.2. Validation of the model using calcium and silicon contents

One key performance indicator to validate the model is the calculated calcium concentration derived from μXRF measurements. Normalized calcium concentrations generated from the simulations, as described in Section 5.2, facilitate a comparative assessment with experimental data on a qualitative and quantitative basis.

Qualitative analysis refers here to identify the distribution and evolution, such as slope and transition zones (concentration drop), of the Ca or Si concentration compared with the experimental results, while in the quantitative analysis the mRMSE is assessed by the deviation of the calculated error.

In Fig. 8, the transmission of the elements, Ca and Si, from the experimentally tested specimen to the extracted data is depicted. Indicated within the bulk material are locations where color transitions occurred. Notably, up to a depth of 2.2 mm, the solid medium was

Fig. 4. Flow chart of the parameter optimization.

fractured, necessitating epoxy resin reinforcement for μXRF analysis. Consequently, to align the data with a reference domain, an adjustment by masking the domain via the mRMSE was executed. This comparison also explains the divergent onsets of the experimental data sets in Figs. 10 and 9.

Experimental findings, shown in Figs. 9 and 10, indicate a good agreement between the model's predictions and experimental results across all time intervals spanning from 35 to 84 days. Notably, the most favorable correspondence is observed at 70 and 77 days, with a nearly exact match evident. This is corroborated by the low mRMSE value (Table 4) and excellent quantitative agreement. Specifically, at 77 days, the smallest mRMSE value is attained in the calcium distribution, accompanied by the best agreement near the attacked interface. This improved consistency shows the enhancement of using multiple C–S–H-phases as mentioned in Section 3.3.1. The simulation demonstrates a more gradual evolution of calcium content, in absence of an abrupt decline in calcium content.

This excellent congruence between the simulation and experiments extends beyond just the quantitative assessment of the overall calcium contents, which may be subjected to normalization influences. Qualitatively, the trends in calcium content, such as curvatures and slopes, exhibit remarkable consistency with experimental observations.

The secondary criterion for validating the model pertains to the silicon content, also in the same time intervals ranging from 35 to 84 days. This variable exhibits greater uncertainty due to the influence of various mineral phases and their thermodynamic characteristics, including individual molar mass and molar volume, which determine the volume and mass fractions in simulation and the results of post-processing. In addition to this inherent complexity arising from the presence of diverse minerals, the data displays a good level of agreement with the experimental findings.

It is important to acknowledge the significant correlation between the normalized Ca and Si concentrations, and the local densities as elucidated in Section 4.1.1. The aforementioned elements' contents are expressed relatively to the total bulk mass, calculated for each computational cell. Consequently, the depicted Si content in Fig. 10 surpasses unity, attributable to an approximately six-fold increase in Si concentration when contrasted to the original bulk material, inclusive of Portlandite.

The biggest deviations can be seen at time step 42 and 84 days. The local increase in Si content between 5 mm and 6 mm at day 42 may be attributed to a more rapid local density variation, as a comparable trend mentioned before at the calcium content.
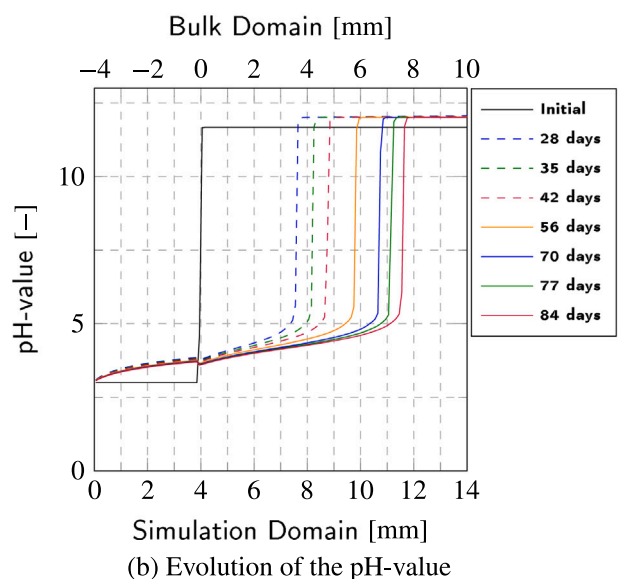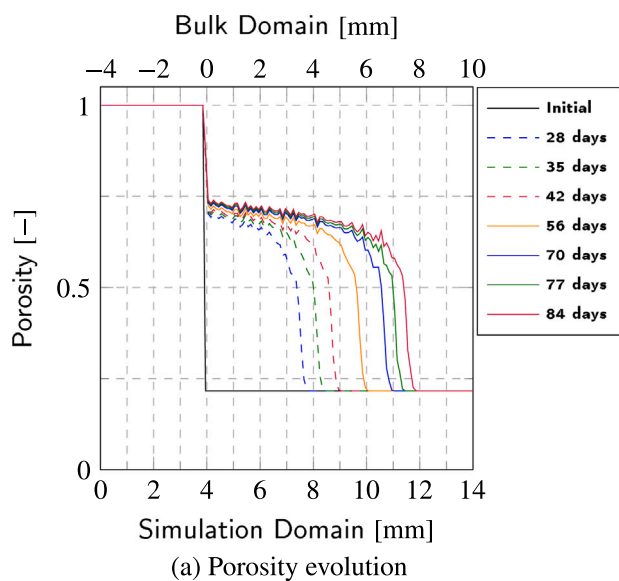
(a) Porosity evolution

(b) Evolution of the pH-value

Fig. 5. Evolution of the porosity and pH-value in the simulation. Simulation Domain according to Fig. 2.

At 84 days, a persistent inconsistency becomes apparent with a continually increasing difference between measured and simulated data. Here the discrepancy is continuously rising, which could point to a faster change in porosity or a faster precipitation of amorphous SiO_2, which has a higher relative Si-content.

6.3. Computational time and error

The presented simulation required an average runtime of approximately 5 min to reach the end time of 84 days. The average time step (variable modified) was around the magnitude of 10^{-3} to 10^{-4} days. This still shows a sufficient efficiency of the single-core computation.

Furthermore, the accuracy of all time steps of Si and Ca-contents was evaluated using the mRMSE. The calcium distribution had a higher accuracy of up to an error of around 6% at two time steps and three time steps could reach an error of below 10%. The elevated uncertainties in silicon distribution can be attributed to the presence of multiple silicon-containing phases and the increased sensitivity to

Table 4
Results of the masked root mean square error.

Time step	X_{min}^{bulk}	X_{max}^{bulk}	mRMSE
Calcium			
35	4.2	8.0	0.067
42	1.0	8.0	0.118
70	2.5	10.0	0.074
77	2.2	10.0	0.061
84	1.5	10.0	0.131
Silicon			
35	4.2	8.0	0.202
42	1.0	8.0	0.546
70	2.5	10.0	0.260
77	2.2	10.0	0.338
84	1.5	10.0	1.075

density variations, resulting in mRMSE that surpass those observed for calcium.

All values of the mRMSE as well as the representative domains $\left(X_{min} \text{ to } X_{max}\right)$ are presented in Table 4.

7. Discussion

In this study, determining material parameters presented a formidable challenge owing to the intricate nature of the system being examined. The contrast between simplified models characterized by restricted parameters and variables, and authentic experimental data generated considerable uncertainties, thereby complicating the process of parameter estimation.

Within the scope of this research, various interactions among several mechanisms occurred during the simulations. The thermodynamic and kinetic behavior of every mineral phase influenced the overall simulation through modifications to local compositions, subsequently impacting transport phenomena (for instance, via alterations in porosity).

This investigation involved modeling the dissolution of diverse C–S–H-phases. Expanding the model to incorporate additional phases and species presents a promising avenue towards a more accurate representation of real systems. However, it introduces further uncertainties. These originate primarily from the substantial number of material parameters that, when obtainable, may have been derived under ideal conditions and hence might not directly be applicable to cementitious systems. Roosz et al. [15] compared OPC degradation by acetic acid with thermodynamic predictions, revealing gaps in Si and Al behavior at low pH. While only amorphous silica and gibbsite were predicted, NMR identified an aluminosilicate gel, prompting the proposal of a new composition and equilibrium constant for this phase.

This data is particularly relevant for blended cements with high-Al pozzolans like metakaolin. However, incorporating such detailed thermodynamic models into reactive transport simulations is challenging. To improve practicality, future models should simplify by reducing the number of involved phases, while still enhancing predictions for modern cement durability in aggressive environments.

The integration of multiple C–S–H-phases marked a substantial advancement towards simulating real-world samples. This progression stems from enhanced porosity evolution resulting from the synergistic effects of distinct C–S–H-phase reactions and their unique reaction kinetics.

7.1. Parameter uncertainties

In the context of model coupling, a significant effect lies in the material parameters, particularly concerning the degradation of C–S–H-phases. The sequential emergence of distinct phases hinges upon their dissolution and precipitation behaviors. Experimental investigations,
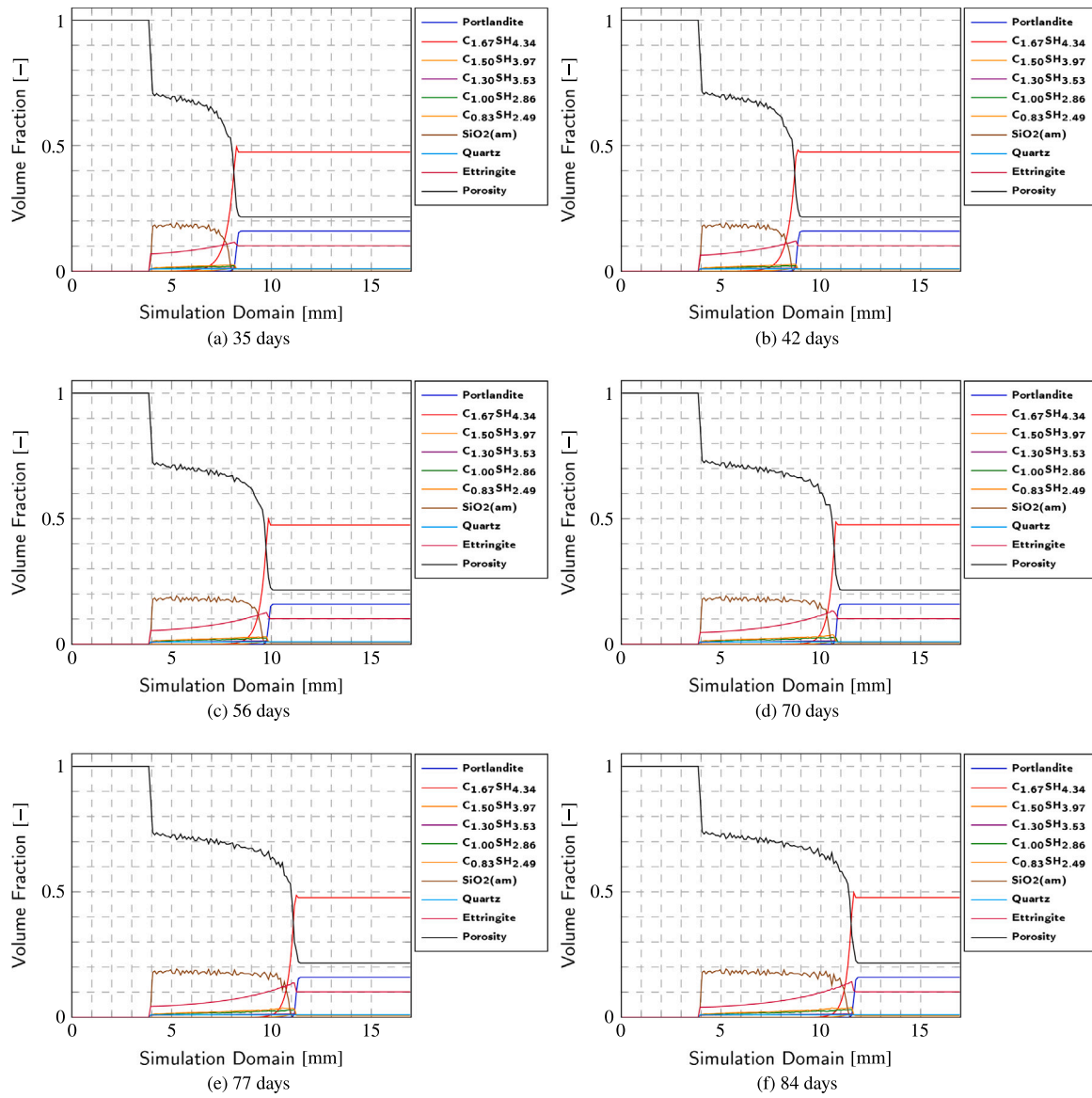
Fig. 6. Assessing mineral phases behavior through normalized volume fractions analysis in a long-term simulation at different time steps between 35 and 84 days. Simulation Domain according to Fig. 2.
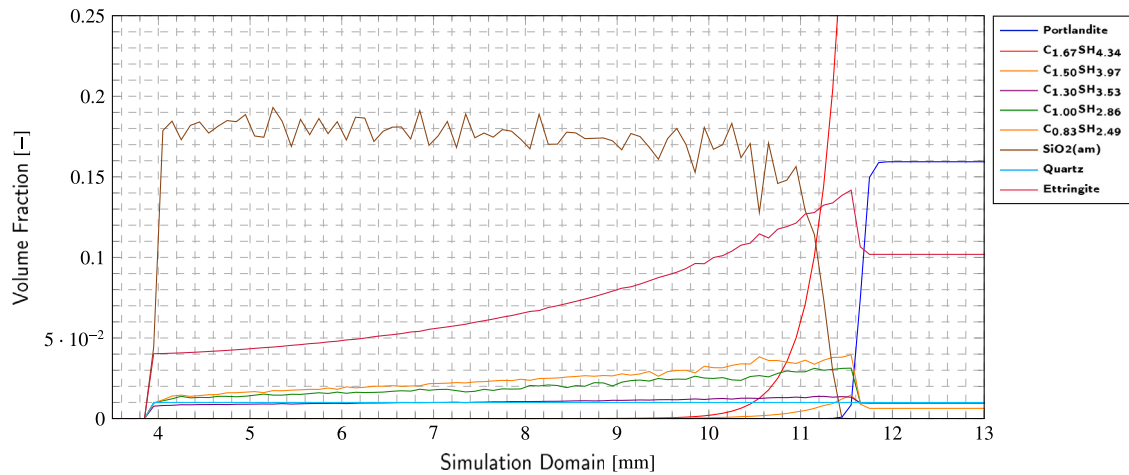

Fig. 7. Assessing mineral phases behavior through normalized volume fractions analysis in a long-term simulation at 84 Days. Simulation Domain according to Fig. 2.
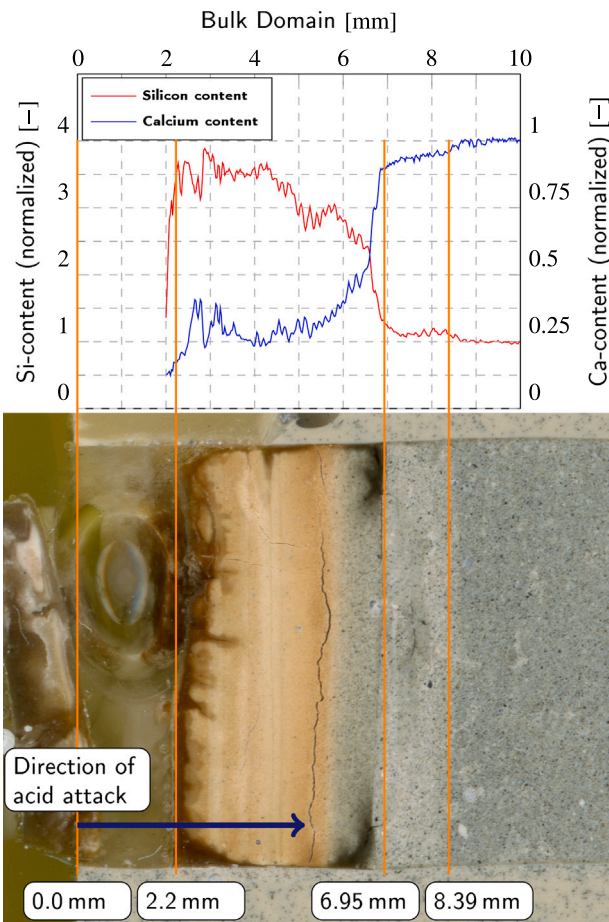
Fig. 8. Extraction of normalized Ca and Si contents from the corresponding test specimen at 77 days determined by μXRF. Gray areas at the top and bottom are initial epoxy coatings prior to the acid attack. The yellow epoxy coating on the left was added after the acid attack. (For interpretation of the references to color in this figure legend, the reader is referred to the web version of this article.)

involving pure phases, serve to elucidate individual parameters; however, such findings do not encapsulate the combined effects in the entire compositional framework. As a result, the extensive array of material parameters harbors inherent uncertainties necessitating optimization processes.

Our examination reveals several influential parameters requiring calibration or approximations. Three most important are here:

- the Specific Surface Area (SSA) and
- the precipitation kinetics of the C–S–H-phases

The value of the SSA was adopted based on dissolution kinetic data presented by Trapote-Barreira et al. [32]. A big divergence exists between the experimental results from Suda et al. [34] and estimations derived from eg. Brunet et al. [21,22] and Zhang et al. [23], which raises two plausible explanations:

First, the SSA reported by Suda et al. [34] for synthetic C–S–H-phases might not mirror the actual surface area engaged in chemical interactions due to the coexistence of clogging phases within the composition. Consequently, the reported SSA values might overestimate the true accessible reactive surface area.

Second, the SSA impacts the dissolution rate via Eq. (6). While the data from Trapote-Barreira et al. [32] might implicitly already account for the SSA, direct incorporation into the dissolution constant might enhance accuracy by reducing two parameters to a single one. Nevertheless, neglecting variations in reactive versus total SSA within the bulk may result in ambiguous parameter values.

Addressing these challenges warrants concurrent determination of both reaction kinetics and real-time SSA throughout the reaction progression. Such an integrated strategy promotes improved comprehension of the role played by SSA in reaction dynamics and facilitates more refined characterization of the system.

The precise precipitation rates of all distinct C–S–H-phases remain the same and only change as a whole. This is due to the absence of experimental data and experimental knowledge of identifying distinct C–S–H-phases in the bulk which complicates the definition of exact precipitation rates for all individual C–S–H-phases.

Lastly, the employed cementation parameter functioned effectively in our model is derived by cement-CO_2 interactions [21,22]. Although subjected to different reactions during acid attacks, it delivered acceptable performance in our investigation but might need further understanding of applicability.

7.2. Post-processing

Based on the obtained μXRF experimental data, the normalized mass fractions of silicon and calcium were derived. The post-processing stage yielded satisfactory outcomes for the extracted components. However, discrepancies emerged between the simulated and experimental findings, particularly concerning the silicon content, are primarily in regions with high porosity. These differences can be attributed to the normalization procedure which is influenced by the porosity. During this process, the total mass fractions are initially accumulated and subsequently adjusted based on the local density. Consequently, variations in porosity lead to increased errors.

Despite these inconsistencies regarding the silicon content, the qualitative comparison displayed excellent agreement between simulations and experiments. Thus, the proposed post-processing procedure remains an appropriate technique for correlating computational results with experimental data from the μXRF.

It should be noted that the experimental data does not provide definitive proof of the existence of distinct C–S–H-phases, which exhibit varying Ca/Si-ratios and significantly influence the silicon content.

7.3. Transport

In transport phenomena, the rate of substance movement is governed by the interplay between the diffusion coefficients and the concentration gradient. The diffusion coefficient is primarily influenced by the porosity and other interacting species.

To elucidate these effects, computational simulations were carried out employing two distinct methodologies. The impact of the NPE was neglected in the first approach, resulting in the assumption of a constant diffusion coefficient throughout the system. Conversely, in the second scenario, a boundary condition (BC) was imposed in close proximity to the initial surface. A comparative analysis of the results obtained using each technique is intended to distinguish the individual contributions of the diffusion coefficient's inherent properties and the concentration gradient's influence on overall transport behavior.

7.3.1. Influence of Nernst–Planck-Equation

To assess the impact of a consistent diffusion coefficient on ion transport, the individually specified diffusion coefficients listed in Table 2, which are used in the Nernst–Planck-Equation (NPE) have been replaced with an uniform averaged value, denoted as $D_{All-const} = 2.01\text{E}-09\,\text{m}^2/\text{s}$. Consequently, the NPE is neglected, and instead, a constant diffusion coefficient is incorporated into Fick's second law (Eq. (1)).

In Fig. 11, the substantial influence of varying diffusion coefficients among the species is evident. While the proposed simulation, including the NPE, reaches a mRMSE of 0.06 for Ca and 0.34 for Si, the same simulation without NPE using the averaged diffusion coefficient can only reach a mRMSE of 0.30 for Ca and 0.74 for Si.
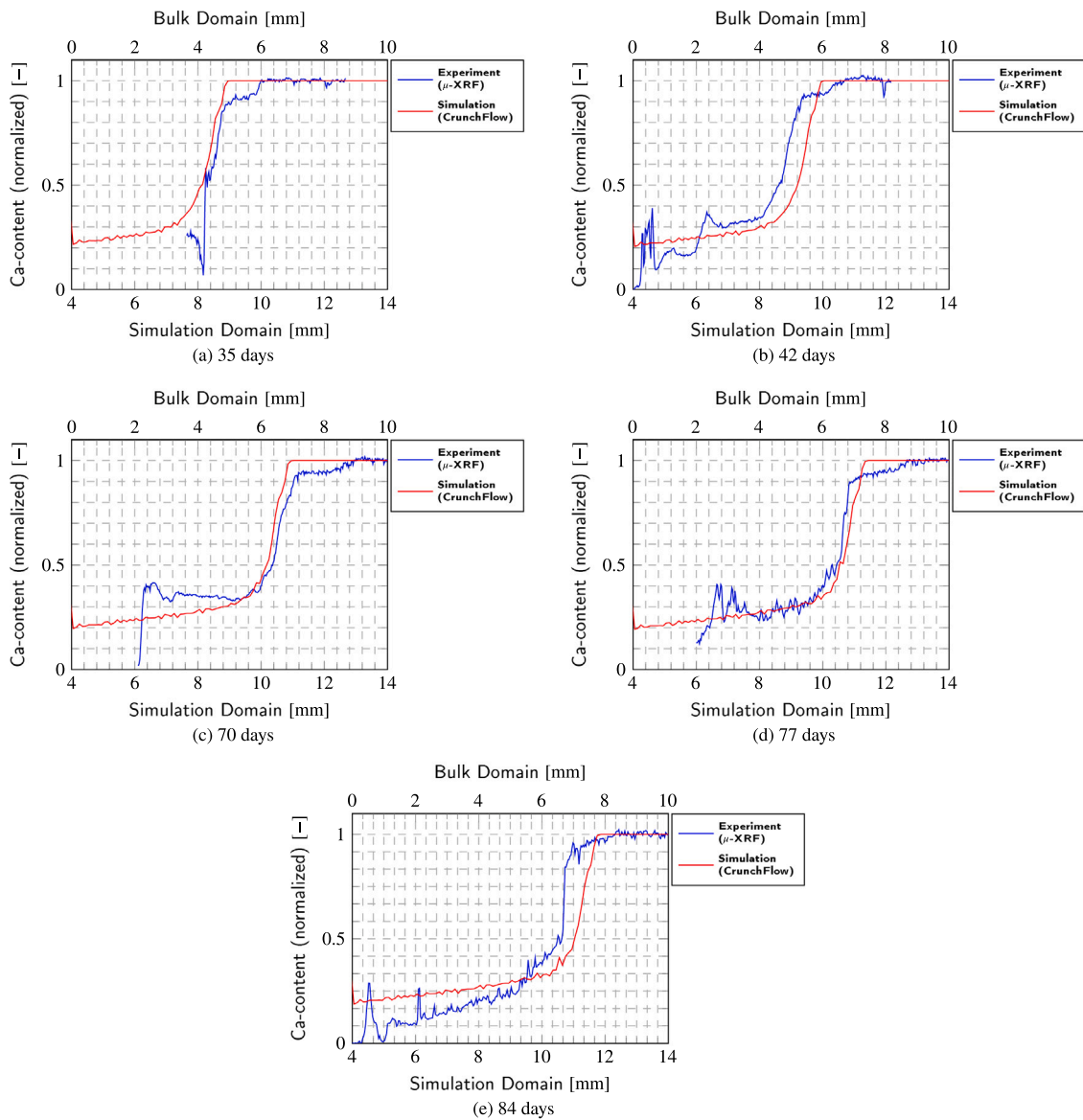
Fig. 9. Comparison of the experimental results from μXRF and the simulation for the Ca^{2+}-concentration at different time steps. Simulation Domain according to Fig. 2.

This effect underscores the necessity of employing the NPE in such simulations to accurately model ion transport. The absence of this consideration led to a further deterioration progression by approximately 2 mm.

It is essential to note that the proposed simulation exhibits a remarkable level of agreement with values obtained from experiments. At the interface, the model demonstrates an almost exact solution at 77 days. The significance of including a detailed composition of the pore solution becomes evident when attempting to simulate the deterioration process. Although the pore solution remains incomplete and simplifications have been made, a high degree of accuracy can nonetheless be attained.

7.3.2. Influence of acidic water domain

During the conducted experimental investigations, a stirred tank apparatus was employed for the experimental studies. Establishing a defined boundary condition (BC) in the simulation at the tank's interface proved challenging due to the movement of the fluid within the vessel. For computational analysis, a liquid domain with dimensions of 4 mm was selected. In order to examine the impact of the location of

this boundary condition on the results, its position was adjusted from 4.0 mm (at x = 0.0 mm) to 1.0 mm (at x = 3.0 mm), situated in proximity to the free surface.

The results of the BC, displayed in Fig. 12, shows that, as it can be predicted: if the BC is set closer to the surface, the concentration gradient becomes greater so the attacked interface moves further. This happens due to the steeper concentration gradient imposed by the fixed BC. It also shows that the chosen distance from the BC to the initial surface of 4 mm gives the best result. Also the results of the mRMSE can quantify this: the chosen 4 mm domain results in a mRMSE of 0.06 for Ca and 0.34 for Si but for the smaller domain of 1 mm could only reach 0.14 for Ca and 0.40 for Si.

Considering the BC it should also be noted that during the experiments the pH-value was set by titrating acetic acid. The solution was repeatedly refreshed at various time points, yet the solution still exhibited minimal variations over this time period, as previously discussed in Section 2.1.1. Therefore also the composition of species changes over time which again has an influence on the chemical reactions by the change of composition.
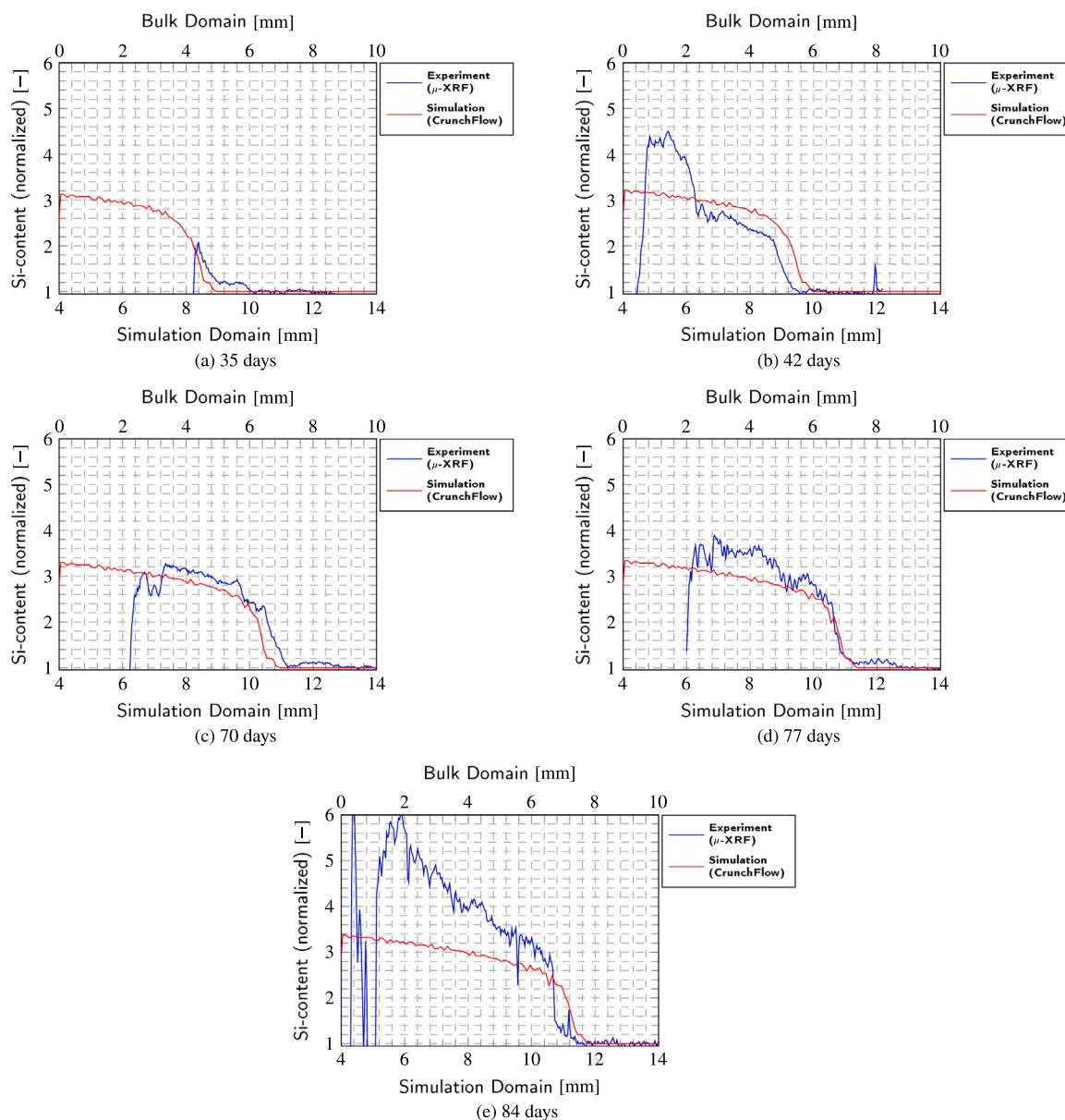
Fig. 10. Comparison of the experimental results from μXRF and the simulation for the Si-concentration at different time steps. Simulation Domain according to Fig. 2.

8. Conclusion

The present study introduces a refined model involving nine mineral phases, enabling the explicit representation of five distinctive C–S–H-phases during degradation of cement-based materials under acetic acid attack. This enhancement facilitates a more precise description of the degradation process, encompassing aspects such as porosity evolution, calcium leaching, and silicon dissolution.

Experimental analysis was conducted on specimens utilizing Micro X-ray Fluorescence (μXRF), revealing their degradation depth dependence. The obtained data was compared with a developed post-processing workflow of the simulation results for a comprehensive comparison between the experimental findings and the proposed model's predictions. The accuracy of the simulation compared with the experimentally determined distributions of calcium (Ca) and silicon (Si) at different time steps was assessed utilizing the masked Root Mean Squared Error (mRMSE) metric, which attained a value as low as 6 %.

The simulations were executed employing primarily material parameters obtained from independent measurements, encompassing diffusion coefficients, solubility products, molar volumes, and dissolution rates. The specific surface area (SSA) and precipitation rate of C–S–H-phases required modification to facilitate phase interactions during the simulation process. The two-order-of-magnitude lower calibrated values compared to theoretical SSA suggests only a small fraction of the C–S–H actively contributes to reaction kinetics. This is attributed to localized reaction boundaries, phase blockages, and microstructural complexity.

The precipitation kinetics of C–S–H-phases necessitate calibration to ensure a sequential phase transitions within these phases. By this adjustment, their formation can be influenced, subsequently impacting the volume fractions and ultimately the porosity.

However, for a more profound comprehension of the reaction kinetic parameters and kinetic aspects governing the acidic attack on cement paste, it is essential to further investigate microstructure dependency of kinetic parameters in future research.
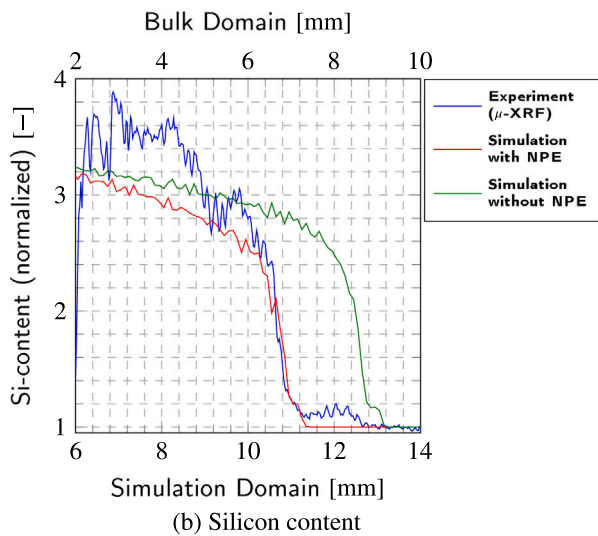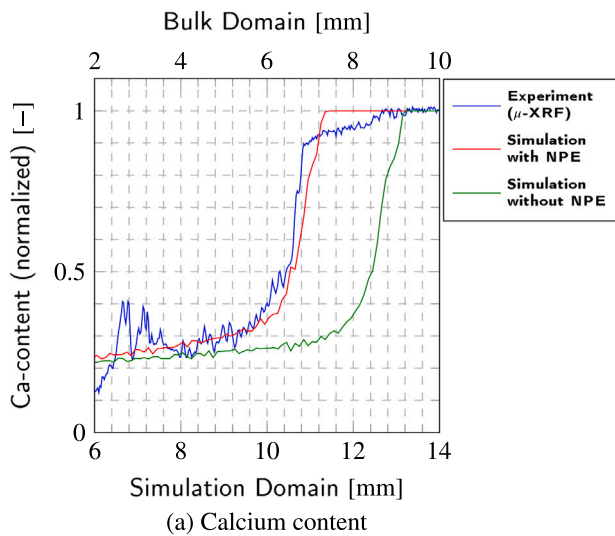
Fig. 11. Influence of the Nernst–Planck-Equation on the Si and Ca content compared with the experimental result at 77 days. Simulation Domain according to Fig. 2.

Fig. 12. Influence of the boundary condition on the Si and Ca content compared with the experimental result at 77 days. Simulation Domain according to Fig. 2.

To address further development of this advanced model, a broader scope of mineral phases and species, such as different types of aluminates as well as iron-containing phases and more complex pore solution, must be incorporated. However, with each added parameter comes inherent uncertainty. Parametric investigations demonstrate the importance of identifying these uncertainties and assessing their influence on changes in material behavior.

In order to facilitate these investigations, advancements in experimental and modeling techniques as well as computational workflows are essential. Sensitivity analyses and optimizations will play a crucial role in calibrating and validating the vast array of parameters, such as local density evolution and distinct precipitation rates for all C–S–H-phases, that arise from incorporating comprehensive material behavior. Also improvements in experimental findings about porosity evolution will help to validate not only the chemical composition but also transport mechanisms. In order to extend the model to 2D and 3D meso-scale mortar and concrete systems, encompassing interconnected multi-component reactions with aggregates, it is essential to employ computationally advanced frameworks. The complexity of these reactive-transpo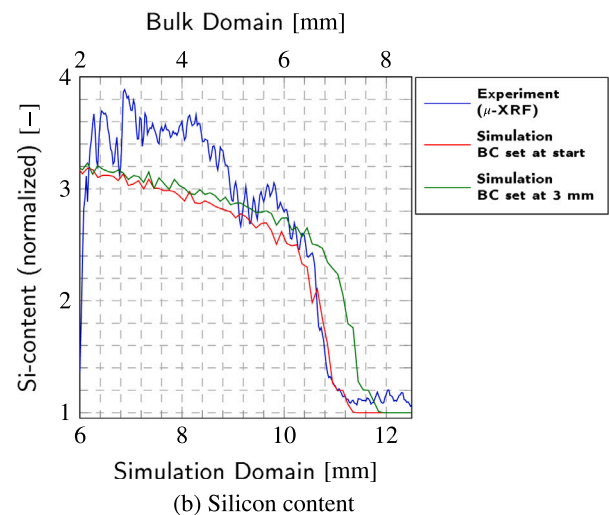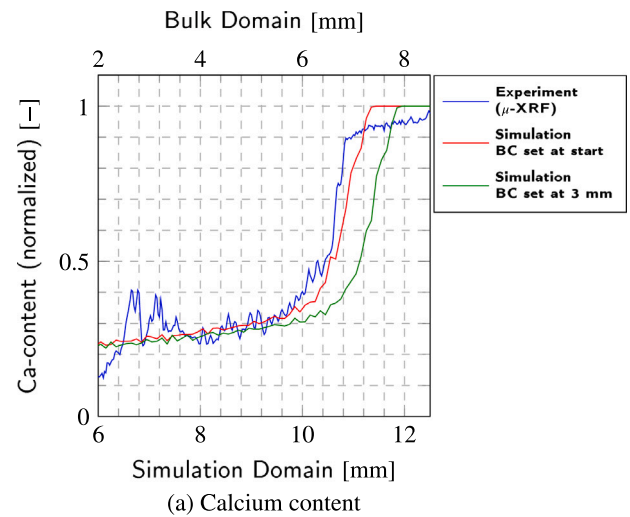rt models for durability extrapolations of cementitious materials necessitates the utilization of parallelized calculation methods to efficiently process large volumes of data and reduce computational time.

CRediT authorship contribution statement

Maximilian Löher: Writing – original draft, Visualization, Validation, Methodology, Investigation, Formal analysis, Conceptualization. **Neven Ukrainczyk:** Writing – review & editing, Validation, Supervision, Conceptualization. **Andreas Bogner:** Writing – review & editing, Methodology, Investigation. **Astrid Hirsch:** Methodology, Investigation. **Frank Dehn:** Resources, Project administration. **Eduardus Koenders:** Resources, Project administration.

Declaration of competing interest

The authors declare that they have no known competing financial interests or personal relationships that could have appeared to influence the work reported in this paper.

Acknowledgments

Appendix A. Supplementary data

Supplementary material related to this article can be found online at https://doi.org/10.1016/j.cemconres.2024.107704.

Data availability

Data will be made available on request.

References

[1] A. Bertron, J. Duchesne, G. Escadeillas, Attack of cement pastes exposed to organic acids in manure, Cem. Concr. Compos. 27 (9–10) (2005) 898–909, http://dx.doi.org/10.1016/j.cemconcomp.2005.06.003.

[2] A. Koenig, F. Dehn, Main considerations for the determination and evaluation of the acid resistance of cementitious materials, Mater. Struct. 49 (5) (2016) 1693–1703, http://dx.doi.org/10.1617/s11527-015-0605-7.

[3] N. Ukrainczyk, M. Muthu, O. Vogt, E. Koenders, Geopolymer, calcium aluminate, and portland cement-based mortars: Comparing degradation using acetic acid, Materials 12 (19) (2019) 3115, http://dx.doi.org/10.3390/ma12193115.

[4] L. De Windt, A. Bertron, S. Larreur-Cayol, G. Escadeillas, Interactions between hydrated cement paste and organic acids: Thermodynamic data and speciation modeling, Cem. Concr. Res. 69 (2015) 25–36, http://dx.doi.org/10.1016/j.cemconres.2014.12.001.

[5] D. Qiao, T. Matsushita, T. Maenaka, R. Shimamoto, Long-term performance assessment of concrete exposed to acid attack and external sulfate attack, J. Adv. Concr. Technol. 19 (7) (2021) 796–810, http://dx.doi.org/10.3151/jact.19.796.

[6] A. Koenig, F. Dehn, Biogenic acid attack on concretes in biogas plants, Biosyst. Eng. 147 (2016) 226–237, http://dx.doi.org/10.1016/j.biosystemseng.2016.03.007.

[7] C. Grengg, F. Mittermayr, N. Ukrainczyk, G. Koraimann, S. Kienesberger, M. Dietzel, Advances in concrete materials for sewer systems affected by microbial induced concrete corrosion: A review, Water Res. 134 (2018) 341–352, http://dx.doi.org/10.1016/j.watres.2018.01.043.

[8] C. Grengg, N. Ukrainczyk, G. Koraimann, B. Mueller, M. Dietzel, F. Mittermayr, Long-term in situ performance of geopolymer, calcium aluminate and Portland cement-based materials exposed to microbially induced acid corrosion, Cem. Concr. Res. 131 (2020) 106034, http://dx.doi.org/10.1016/j.cemconres.2020.106034.

[9] H. Yuan, P. Dangla, P. Chatellier, T. Chaussadent, Degradation modeling of concrete submitted to biogenic acid attack, Cem. Concr. Res. 70 (2015) 29–38, http://dx.doi.org/10.1016/j.cemconres.2015.01.002.

[10] F. Berger, A. Bogner, A. Hirsch, N. Ukrainczyk, F. Dehn, E. Koenders, Thermodynamic modeling and experimental validation of acetic acid attack on hardened cement paste: Effect of silica fume, Materials 15 (23) (2022) 8355, http://dx.doi.org/10.3390/ma15238355.

[11] R.E. Beddoe, H.W. Dorner, Modelling acid attack on concrete: Part I. The essential mechanisms, Cem. Concr. Res. 35 (12) (2005) 2333–2339, http://dx.doi.org/10.1016/j.cemconres.2005.04.002.

[12] J. Perko, N. Ukrainczyk, B. Šavija, Q.T. Phung, E.A.B. Koenders, Influence of micro-pore connectivity and micro-fractures on calcium leaching of cement pastes—A coupled simulation approach, Materials 13 (12) (2020) 2697, http://dx.doi.org/10.3390/ma13122697.

[13] A. Koenig, F. Dehn, Biogenic acid attack on concretes in biogas plants, Biosyst. Eng. 147 (2016) 226–237, http://dx.doi.org/10.1016/j.biosystemseng.2016.03.007.

[14] C.S. Walker, S. Sutou, C. Oda, M. Mihara, A. Honda, Calcium silicate hydrate (C-S-H) Gel solubility data and a discrete solid phase model at 25 °C based on two binary non-ideal solid solutions, Cem. Concr. Res. 79 (2016) 1–30, http://dx.doi.org/10.1016/j.cemconres.2015.07.006.

[15] C. Roosz, M. Giroudon, L. Lacarrière, M. Peyre Lavigne, C. Patapy, A. Bertron, New insights into aluminosilicate gel from acetic acid attack of hydrated Portland cement: Experimental and thermodynamic characterization, Appl. Geochem. 162 (2024) 105923, http://dx.doi.org/10.1016/j.apgeochem.2024.105923.

[16] T. Dyer, Influence of cement type on resistance to attack from two carboxylic acids, Cem. Concr. Compos. 83 (2017) 20–35, http://dx.doi.org/10.1016/j.cemconcomp.2017.07.004.

[17] M. Addassi, V. Marcos-Meson, W. Kunther, H. Hoteit, A. Michel, A methodology for optimizing the calibration and validation of reactive transport models for cement-based materials, Materials 15 (16) (2022) 5590, http://dx.doi.org/10.3390/ma15165590.

[18] S. Sharmilan, H. Stang, A. Michel, A multi-species reactive transport model based on ion-solid phase interaction for saturated cement-based materials, Cem. Concr. Res. 159 (2022) 106861, http://dx.doi.org/10.1016/j.cemconres.2022.106861.

[19] H. Yuan, P. Dangla, P. Chatellier, T. Chaussadent, Degradation modelling of concrete submitted to sulfuric acid attack, Cem. Concr. Res. 53 (2013) 267–277, http://dx.doi.org/10.1016/j.cemconres.2013.08.002.

[20] Steefel, CrunchFlow manual, 2009.

[21] J.-P.L. Brunet, L. Li, Z.T. Karpyn, B.G. Kutchko, B. Strazisar, G. Bromhal, Dynamic evolution of cement composition and transport properties under conditions relevant to geological carbon sequestration, Energy Fuels 27 (8) (2013) 4208–4220, http://dx.doi.org/10.1021/ef302023v.

[22] J.-P.L. Brunet, L. Li, Z.T. Karpyn, N.J. Huerta, Fracture opening or self-sealing: Critical residence time as a unifying parameter for cement–CO2–brine interactions, Int. J. Greenh. Gas Control 47 (2016) 25–37, http://dx.doi.org/10.1016/j.ijggc.2016.01.024.

[23] L. Zhang, D.A. Dzombak, D.V. Nakles, J.-P.L. Brunet, L. Li, Reactive transport modeling of interactions between acid gas (CO2 + H2S) and pozzolan-amended wellbore cement under geologic carbon sequestration conditions, Energy Fuels 27 (11) (2013) 6921–6937, http://dx.doi.org/10.1021/ef401749x.

[24] R. Caron, R.A. Patel, A. Bogner, F. Dehn, Multi-scale experimental investigation and analytical micro-mechanical modeling to determine the elastic properties of alkali activated concrete, SSRN Electron. J. (2022) http://dx.doi.org/10.2139/ssrn.4175926.

[25] K.T. MacQuarrie, K.U. Mayer, Reactive transport modeling in fractured rock: A state-of-the-science review, Earth-Sci. Rev. 72 (3–4) (2005) 189–227, http://dx.doi.org/10.1016/j.earscirev.2005.07.003.

[26] C.I. Steefel, C.A.J. Appelo, B. Arora, D. Jacques, T. Kalbacher, O. Kolditz, V. Lagneau, P.C. Lichtner, K.U. Mayer, J.C.L. Meeussen, S. Molins, D. Moulton, H. Shao, J. Šimůnek, N. Spycher, S.B. Yabusaki, G.T. Yeh, Reactive transport codes for subsurface environmental simulation, Comput. Geosci. 19 (3) (2015) 445–478, http://dx.doi.org/10.1007/s10596-014-9443-x.

[27] B. Lothenbach, D.A. Kulik, T. Matschei, M. Balonis, L. Baquerizo, B. Dilnesa, G.D. Miron, R.J. Myers, Cemdata18: A chemical thermodynamic database for hydrated Portland cements and alkali-activated materials, Cem. Concr. Res. 115 (2019) 472–506, http://dx.doi.org/10.1016/j.cemconres.2018.04.018.

[28] E. Samson, J. Marchand, Modelling ion diffusion mechanisms in porous media, 1999, p. 18.

[29] C.I. Steefel, A.C. Lasaga, A coupled model for transport of multiple chemical species and kinetic precipitation/dissolution reactions with application to reactive flow in single phase hydrothermal systems, Am. J. Sci. 294 (5) (1994) 529–592, http://dx.doi.org/10.2475/ajs.294.5.529.

[30] N.C. Marty, C. Tournassat, A. Burnol, E. Giffaut, E.C. Gaucher, Influence of reaction kinetics and mesh refinement on the numerical modelling of concrete/clay interactions, J. Hydrol. 364 (1–2) (2009) 58–72, http://dx.doi.org/10.1016/j.jhydrol.2008.10.013.

[31] J. Liaudat, A. Martínez, C.M. López, I. Carol, Modelling acid attack of oilwell cement exposed to carbonated brine, Int. J. Greenh. Gas Control 68 (2018) 191–202, http://dx.doi.org/10.1016/j.ijggc.2017.11.015.

[32] A. Trapote-Barreira, J. Cama, J.M. Soler, Dissolution kinetics of C–S–H Gel: Flow-through experiments, Phys. Chem. Earth A/B/C 70–71 (2014) 17–31, http://dx.doi.org/10.1016/j.pce.2013.11.003.

[33] J. Ganguly, Thermodynamic modelling of solid solutions, in: G. Papp, T.G. Weiszburg, C.A. Geiger (Eds.), Solid Solutions in Silicate and Oxide Systems, Mineralogical Society of Great Britain and Ireland, Budapest, 2001, pp. 37–69, http://dx.doi.org/10.1180/EMU-notes.3.3.

[34] Y. Suda, T. Saeki, T. Saito, Relation between chemical composition and physical properties of C-S-H Generated from cementitious materials, J. Adv. Concr. Technol. 13 (5) (2015) 275–290, http://dx.doi.org/10.3151/jact.13.275.

[35] J.J. Beisman, R.M. Maxwell, A.K. Navarre-Sitchler, C.I. Steefel, S. Molins, ParCrunchFlow: An efficient, parallel reactive transport simulation tool for physically and chemically heterogeneous saturated subsurface environments, Comput. Geosci. 19 (2) (2015) 403–422, http://dx.doi.org/10.1007/s10596-015-9475-x.

[36] P.C. Lichtner, Chapter 1: Continuum formulation of multicomponent–multiphase reactive transport, Rev. Mineral. 34 (1996).

[37] C.I. Steefel, K.T.B. MacQuarrie, Chapter 2. approaches to modeling of reactive transport in porous media, in: P.C. Lichtner, C.I. Steefel, E.H. Oelkers (Eds.), Reactive Transport in Porous Media, De Gruyter, 1996, pp. 83–130, http://dx.doi.org/10.1515/9781501509797-005.

[38] P.C. Lichtner, Continuum model for simultaneous chemical reactions and mass transport in hydrothermal systems, Geochim. Cosmochim. Acta 49 (3) (1985) 779–800, http://dx.doi.org/10.1016/0016-7037(85)90172-3.

[39] D.G. Leaist, P.A. Lyons, Diffusion in dilute aqueous acetic acid solutions at 25°C, J. Solut. Chem. 13 (2) (1984) 77–85, http://dx.doi.org/10.1007/BF00646041.

[40] T. Sugiyama, W. Ritthichauy, Y. Tsuji, Simultaneous transport of chloride and calcium ions in hydrated cement systems, J. Adv. Concr. Technol. 1 (2) (2003) 127–138, http://dx.doi.org/10.3151/jact.1.127.